Dynamic focal plane estimation for dental panoramic radiography

Seungeon Kim, and Jong Beom Ra[a)]
School of Electrical Engineering, KAIST, Daejeon, Republic of Korea

(Received 11 February 2019; revised 2 September 2019; accepted for publication 3 September 2019; published xx xxxx xxxx)

Purpose: The digital panoramic radiography is widely used in dental clinics and provides the anatomical information of the intraoral structure along the predefined arc-shaped path. Since the intraoral structure varies depending on the patient, however, it is nearly impossible to design a common and static focal path or plane fitted to the dentition of all patients. In response, we introduce an imaging algorithm for digital panoramic radiography that can provide a focused panoramic radiographic image for all patients, by automatically estimating the best focal plane for each patient.
Methods: The aim of this study is to improve the image quality of dental panoramic radiography based on a three-dimensional (3D) dynamic focal plane. The plane is newly introduced to represent the arbitrary 3D intraoral structure of each patient. The proposed algorithm consists of three steps: preprocessing, focal plane estimation, and image reconstruction. We first perform preprocessing to improve the accuracy of focal plane estimation. The 3D dynamic focal plane is then estimated by adjusting the position of the image plane so that object boundaries in the neighboring projection data are aligned or focused on the plane. Finally, a panoramic radiographic image is reconstructed using the estimated dynamic focal plane.
Results: The proposed algorithm is evaluated using a numerical phantom dataset and four clinical human datasets. In order to examine the image quality improvement owing to the proposed algorithm, we generate panoramic radiographic images based on a conventional static focal plane and estimated 3D dynamic focal planes, respectively. Experimental results show that the image quality is dramatically improved for all datasets using the 3D dynamic focal planes that are estimated from the proposed algorithm.
Conclusions: We propose an imaging algorithm for digital panoramic radiography that provides improved image quality by estimating dynamic focal planes fitted to each individual patient's intraoral structure. [https://doi.org/10.1002/mp.13823]

Key words: dental x-ray imaging, digital panoramic radiography, dynamic focal plane, focal plane estimation, image enhancement

1. INTRODUCTION

Digital panoramic radiography has been widely used in dental clinics because it can immediately provide a clinical dental image of a broad range of the jaw with a low radiation dose.[1–6] In particular, the objects of interest, such as the teeth, residing on a focal plane, or focal trough, are clearly observed in the panoramic radiographic image, while the other objects out of the focal plane are blurred. Digital panoramic radiography thereby improves diagnostic accuracy, compared to the conventional X-ray projection radiography.

In a conventional panoramic radiographic imaging system, the projection data are acquired at each view angle using a rotating x-ray source and narrow slit detector pair around sliding rotation centers.[3] A panoramic radiographic image is then obtained by shifting each projection data by predefined amounts and accumulating them. Note that the shift amounts at each projection view angle are calculated so that an object of interest on the focal plane could be accumulated at the same position in the panoramic radiographic image. Therefore, the object on the focal plane appears focused in a panoramic radiographic image, while the one outside the focal plane appears blurred. In general, the focal plane is empirically designed as an arch shape for describing the normal dentition, and the scan trajectory of the source detector pair is correspondingly determined at each projection view angle, while sliding the rotation center.

As mentioned, a panoramic radiographic image is obtained by focusing only the objects residing on a predefined focal plane. Therefore, in order to provide diagnostic image quality for the intraoral structure of a patient, the dentition of the patient should coincide with the focal plane.[3–7] Since the intraoral structure varies depending on the patient, however, it is nearly impossible to determine a focal plane that is commonly fitted to all different dentitions of patients. In some cases, the patient's dentition may deviate significantly from the predefined focal plane, resulting in image quality degradation of a panoramic radiographic image, which may cause misdiagnosis.

Recently, a couple of algorithms that acquire a focused panoramic radiographic image automatically have been reported.[4,6,7] In those algorithms, multiple panoramic radiographic images are first obtained at different layers with various depths,[3,8] and then focused patches are selected from the multiple images based on a sharpness metric. By stitching the selected patches[6] or performing the oriented planar image

reconstruction,[4,7] a focused panoramic radiographic image is obtained. Since these algorithms are based on patch selection among the patches with different depths; however, they accompany a potential risk of unnatural artifacts near the patch boundary, and the focusing accuracy may be bounded by the patch size for the sharpness measurement.

In this paper, we propose a novel algorithm to obtain a focused panoramic radiographic image by directly estimating a 3D focal plane for a given patient. In the proposed algorithm, the 3D dynamic focal plane is newly introduced. The focal plane is then estimated on the basis of the matching among the projection data of different view angles for each patient. The panoramic radiographic image is then reconstructed using the estimated patient-specific focal plane.

The remainder of this paper is organized as follows. In Section 2, the overall structure of the proposed algorithm is given and details of each module are described. In Section 3, experimental results are provided for a numerical phantom and clinical datasets. A discussion and conclusions are given in Sections 4 and 5, respectively.

2. MATERIALS AND METHODS

For the focal plane estimation, we first consider the relationship between the position of the focal plane and the image quality of a panoramic radiographic image. Figure 1(a) shows the data acquisition procedure for an object of interest, where a source-detector pair is used at two different view angles. As shown in Fig. 1(b), the object can be either focused or blurred depending on the position of the accumulated plane. Based on this observation, in order to obtain a focused panoramic radiographic image, we propose a novel algorithm for estimating the focal plane where back-projected boundaries of the objects of interest are well aligned for all view angles.

2.A. Focal plane estimation

2.A.1. Preprocessing

The proposed algorithm estimates a focal plane based on the 2D registration of object boundaries among the back-projected data at different view angles. In addition to the objects of interest, however, the back-projected data include the boundary information of background objects, which mostly lie on the opposite side of the objects of interest with respect to a rotation center. Hence, the background objects have completely different registration relationships from the objects of interest, and thereby tend to make the focal plane estimation less reliable. In response, we preprocess the projection data prior to back-projection, for more accurate and reliable focal plane estimation by reducing the effect of background objects.

For preprocessing, as shown in Fig. 2, we first apply a log-transform to the acquired projection data to obtain line integral values of attenuation coefficients, g.[9,10] We subsequently reconstruct a 3D image, I, using the conventional FDK algorithm.[11] Note that in image I the back-projection is performed only for the region between the detector and the rotation center, where the objects of interest are located. In order to determine whether the 3D position of each voxel, $\mathbf{x}$, is in between the rotation center and the detector at view angle ϕ_i, we use the following equation:

$$S_{\phi_i}(\mathbf{x}) = \left(\mathbf{x} - \mathbf{r}_{\phi_i}\right) \cdot \mathbf{b}_{\phi_i}, \tag{1}$$

where $\mathbf{r}_{\phi_i}$ denotes the 3D position vector of the rotation center of the source-detector pair at view angle ϕ_i, and $\mathbf{b}_{\phi_i}$ denotes a unit vector along the direction from the detector center to source at view angle ϕ_i, as shown in Fig. 2. If $S_{\phi_i}(\mathbf{x})$ is a negative value, $\mathbf{x}$ is considered to reside in between the rotation center and the detector. Even though tooth objects cannot be reconstructed completely due to limited view angles, it is observed in I that object boundaries perpendicular to the projection direction can be well defined.[12–14] In order to reduce the intensity inhomogeneity due to the data truncation arising from small detector width, the intensity value of each voxel in I is normalized using the angular span applied for the back-projection to the corresponding voxel, and the normalized 3D image is illustrated as I_N. We then obtain the simulated projection data, G, by forward projecting I_N only from the rotation center to the detector, or only for the active region, at each view angle. Thereby, the objects of interest are emphasized in G, while background objects are de-emphasized. Finally, in order to make the following projection data alignment procedure more sensitive to

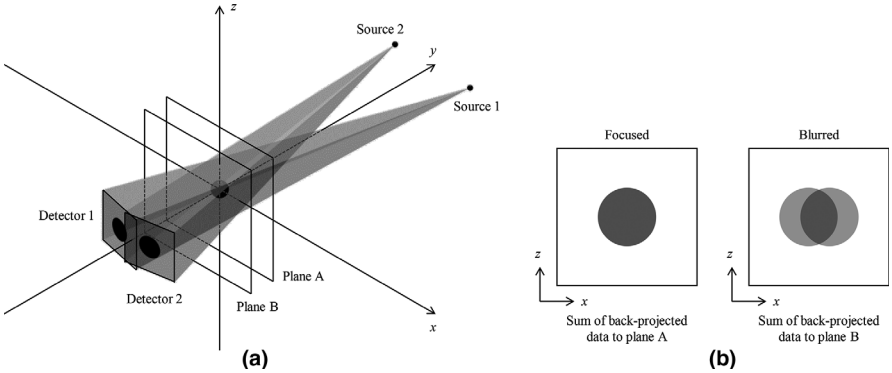

FIG. 1. (a) Projection data acquisition of an object of interest at two different view angles. (b) The object becomes focused or blurred in a panoramic radiographic image depending on whether the object is placed on the focal plane.

object boundaries, we preprocess G using a 1D Laplacian filter and obtain the preprocessed projection data, P.

2.A.2. Dynamic focal plane

In constituting a panoramic radiographic image in an ordinary system, the imaging focal plane is usually set to be static and may thereby cause out of focus areas depending on the patient. Instead of using this static and patient-independent focal plane, we suggest using a patient-dependent dynamic focal plane, where all object boundaries are focused.

Figure 3 conceptually illustrates the proposed method to derive a dynamic focal plane from the initial static focal plane, which is a set of voxel points placed according to the predefined fixed distance ratio from the source to the detector plane. Note here that the static focal plane and the corresponding scanning geometry of the source-detector pair are assumed to be available in the imaging system. Let us assume that a 2D pixel position in a panoramic radiographic image, $\mathbf{x}_{\text{pano}}$, corresponds to a 3D voxel position $\mathbf{x}_{\text{s}}$ on the initial focal plane. We then consider that the voxel position $\mathbf{x}_{\text{d}}$ on the dynamic focal plane can be determined by properly refining $\mathbf{x}_{\text{s}}$.

By adopting a B-spline based 2D interpolation model,[15] the dynamic focal plane can then be described as follows:

$$\mathbf{T}(\mathbf{x}_{\text{pano}};\Theta) = \mathbf{T}(\mathbf{x}_{\text{pano}};\Theta=\mathbf{0}) + \mathbf{v}(\mathbf{x}_{\text{pano}})\sum_{\mathbf{j}} B\left(\frac{\mathbf{x}_{\text{pano}}}{d_s}-\mathbf{j}\right)\theta_{\mathbf{j}}, \tag{2}$$

where

$$\mathbf{T}(\mathbf{x}_{\text{pano}};\Theta)=\mathbf{x}_{\text{d}}, \text{ and } \mathbf{T}(\mathbf{x}_{\text{pano}};\Theta=\mathbf{0})=\mathbf{x}_{\text{s}}. \tag{3}$$

In Eq. (2), Θ denotes a set of L different $\theta_{\mathbf{j}}$, each of which denotes a 2D B-spline coefficient at knot $\mathbf{j}$ in the 2D panoramic radiographic image domain, B denotes the 2D tensor product of 1D cubic B-splines, and d_{s} is a knot interval in the space domain. Hence, the total number of knots, or control points, L, is $\{\lceil (N_x/2)/d_{\text{s}}\rceil \times 2+3\}\times\{\lceil (N_y/2)/d_{\text{s}}\rceil \times 2+3\}$ for a 2D panoramic radiographic image of $N_x \times N_y$ pixels, where $\lceil\cdot\rceil$ denotes the ceiling operator. Note in Fig. 3 that $\theta_{\mathbf{j}}$ are illustrated for the example case of $L = 15$. Also, $\mathbf{v}(\mathbf{x}_{\text{pano}})$ denotes a unit vector for the refinement of $\mathbf{T}(\mathbf{x}_{\text{pano}};\Theta=\mathbf{0})$ and can be obtained using a set of 3D unit vectors from the source to array elements on the detector center column at each view angle. Thereby, a dynamic focal plane can be described using Θ.

2.A.3. Definition of the cost function

In order to determine the optimal control point parameters, $\theta_{\mathbf{j}}$, which can align the object boundaries back-projected from different view angles to the focal plane, we define a data term as the sum of differences between a pair of back-projected data to the focal plane from neighboring view angles. Namely,

$$D(\Theta)=\sum_i \sum_{\mathbf{x}_{\text{pano}}\in\Omega_i} \left\| P_{\phi_i}\left(\mathbf{A}_{\phi_i}\left(\mathbf{T}(\mathbf{x}_{\text{pano}};\Theta)-\mathbf{r}_{\phi_i}\right)\right) - P_{\phi_{i+F}}\left(\mathbf{A}_{\phi_{i+F}}\left(\mathbf{T}(\mathbf{x}_{\text{pano}};\Theta)-\mathbf{r}_{\phi_{i+F}}\right)\right)\right\|_2^2, \tag{4}$$

where P_{ϕ_i} denotes the preprocessed projection data at view angle ϕ_i. In addition, Ω_i is a set of pixel positions, where the back-projected data from view angles of i and $i + F$ are overlapping in the 2D panoramic radiographic image domain. Here, F denotes the view index interval for the comparison of projection data, and an interval of 5 is used in this study.

Figure 4 shows the illustration of back-projection onto an arbitrary point, $\mathbf{x}_{\text{d}}$, [or $\mathbf{T}(\mathbf{x}_{\text{pano}};\Theta)$ in Eq. (4)] in the dynamic

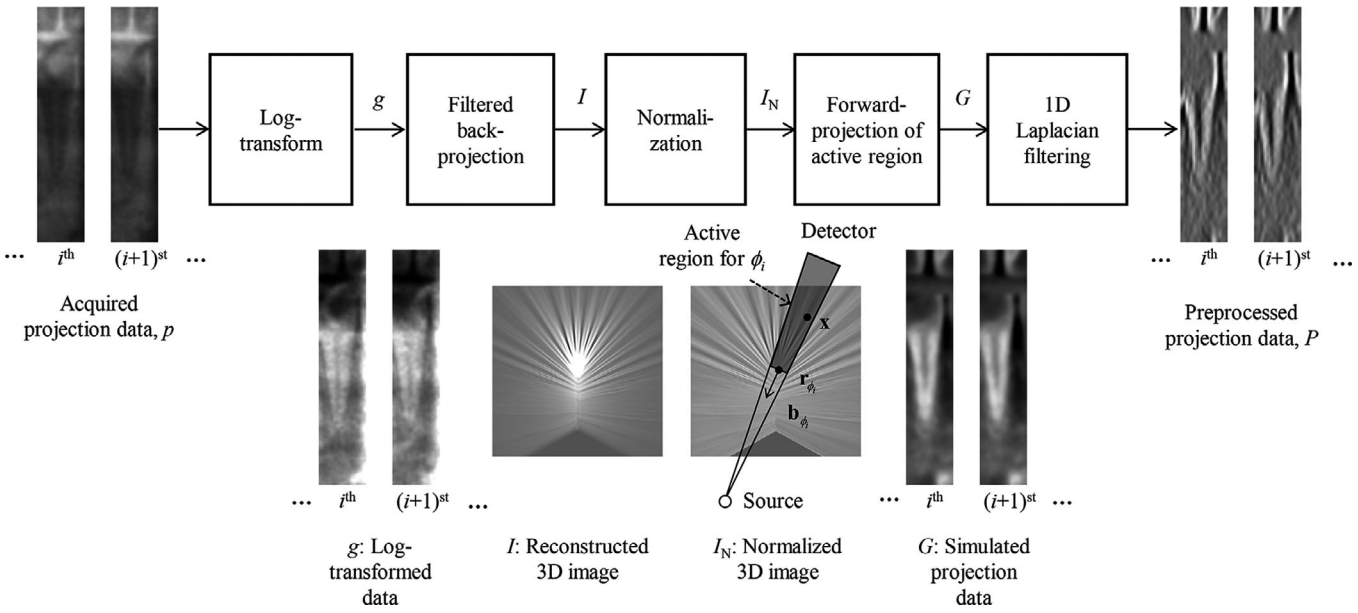

FIG. 2. Flowchart of the proposed preprocessing method.

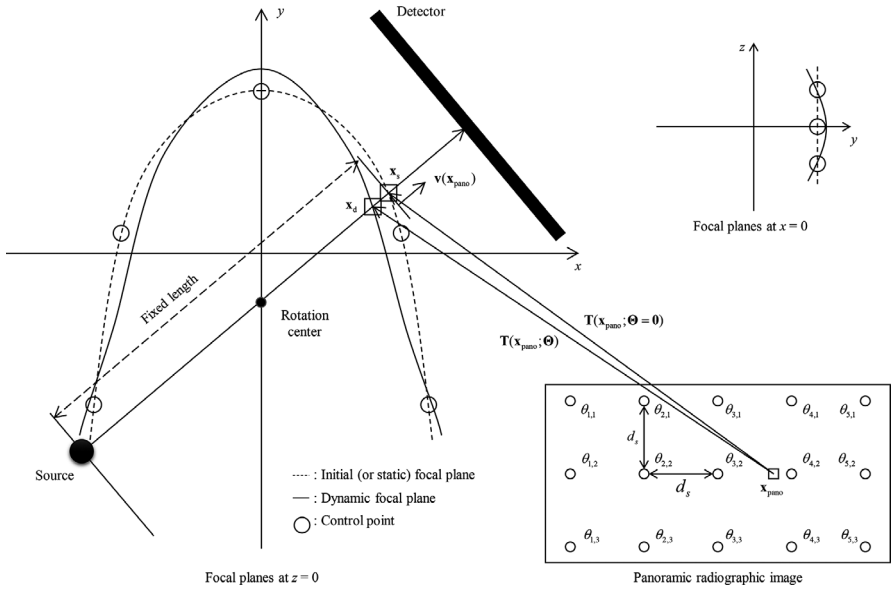

FIG. 3. An example illustration for describing the relationship between point $\mathbf{x}_{\text{pano}}$ on a two-dimensional (2D) panoramic radiographic image and the corresponding point $\mathbf{x}_{\text{d}}$ which is considered to belong to the dynamic focal plane. By determining $\mathbf{x}_{\text{d}}$ for all different view angles, a dynamic focal plane can be described. Note that $\theta_{\mathbf{j}}$ in the 2D panoramic radiographic image domain denotes a 2D *B*-spline coefficient at control point $\mathbf{j}$.

focal plane, at view angle ϕ_i, as an example. Note here that $\mathbf{r}_{\phi_i}$ and $\mathbf{b}_{\phi_i}$ are the same notations described in Fig. 2. As shown in Fig. 4, $\mathbf{A}_{\phi_i}$ is the mapping function from 3D coordinates $\mathbf{x}_{\text{d}}$ to the 2D detector coordinates at ϕ_i, which can be written as follows:

$$\mathbf{A}_{\phi_i}\left(\mathbf{x}_{\text{d}} - \mathbf{r}_{\phi_i}\right) = \frac{R_{\text{SDD}}}{R_{\text{SAD}} - \left(\mathbf{x}_{\text{d}} - \mathbf{r}_{\phi_i}\right) \cdot \mathbf{b}_{\phi_i}} \begin{bmatrix} \left(\mathbf{x}_{\text{d}} - \mathbf{r}_{\phi_i}\right) \cdot \mathbf{a}_{\phi_i} & \left(\mathbf{x}_{\text{d}} - \mathbf{r}_{\phi_i}\right) \cdot \mathbf{a}_z \end{bmatrix}^T. \tag{5}$$

Here, R_{SDD} and R_{SAD} denote the distances from the source to detector and to $\mathbf{r}_{\phi_i}$, respectively. Also, $\mathbf{a}_z$ denotes the unit vector along the z-axis, $\mathbf{a}_{\phi_i}$ represents a unit vector orthogonal to $\mathbf{a}_z$ and $\mathbf{b}_{\phi_i}$, and the superscript T denotes the transpose.

In addition to the data term, we adopt a regularization term for robust parameter estimation by penalizing the excessive difference between neighboring parameters, as follows:

$$R(\Theta) = \sum_{\mathbf{j}} \sum_{\mathbf{k} \in K_{\mathbf{j}}} \left\| \theta_{\mathbf{j}} - \theta_{\mathbf{k}} \right\|_2^2, \tag{6}$$

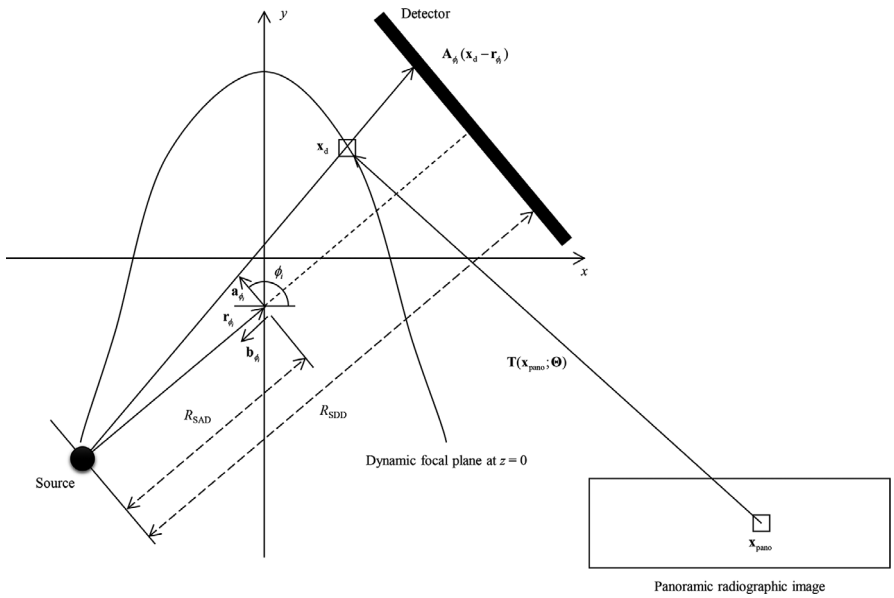

FIG. 4. An illustration of back-projection onto $\mathbf{x}_{\text{d}}$ from the projection data at view angle ϕ_i.

where $K_{\mathbf{j}}$ is a set of knot indices neighboring knot $\mathbf{j}$. Using Eqs. (4) and (6), we define a cost function C as $(D + \lambda R)$, where λ is a regularization parameter. The optimum parameters can then be determined by minimizing C, namely,

$$\Theta = \underset{\Theta}{\operatorname{argmin}}\{C(\Theta)\} = \underset{\Theta}{\operatorname{argmin}}\{D(\Theta) + \lambda R(\Theta)\}. \tag{7}$$

2.A.4. Optimization

The optimal parameters, which minimize C in Eq. (7), can be determined in an iterative manner, based on both the Gauss-Newton method[16,17] and the optimization transfer method.[18–20] Using the Gauss-Newton method, the optimum update amount at iteration step l can be determined as follows:

$$\Delta\hat{\Theta} = \underset{\Delta\Theta}{\operatorname{argmin}}\left\{D\left(\Theta^l + \Delta\Theta\right) + \lambda R\left(\Theta^l + \Delta\Theta\right)\right\}. \tag{8}$$

For the linearization of D, we first rewrite Eqs. (2) and (5) as follows:

$$\mathbf{T}\left(\mathbf{x}_{\text{pano}}; \Theta^l + \Delta\Theta\right) = \mathbf{x}_{\text{d}}^l + \Delta\mathbf{x}_{\text{d}}, \tag{9}$$

and

$$\begin{aligned}\mathbf{A}_{\phi_i}\left(\mathbf{x}_{\text{d}}^l - \mathbf{r}_{\phi_i} + \Delta\mathbf{x}_{\text{d}}\right) = &\frac{R_{\text{SDD}}}{R_{\text{SAD}} - \left(\mathbf{x}_{\text{d}}^l - \mathbf{r}_{\phi_i}\right)\cdot\mathbf{b}_{\phi_i} - \Delta\mathbf{x}_{\text{d}}\cdot\mathbf{b}_{\phi_i}} \\ &\left[\left(\mathbf{x}_{\text{d}}^l - \mathbf{r}_{\phi_i} + \Delta\mathbf{x}_{\text{d}}\right)\cdot\mathbf{a}_{\phi_i} \right. \\ &\left.\left(\mathbf{x}_{\text{d}}^l - \mathbf{r}_{\phi_i} + \Delta\mathbf{x}_{\text{d}}\right)\cdot\mathbf{a}_z\right]^T\end{aligned} \tag{10}$$

where

$$\begin{aligned}\mathbf{x}_{\text{d}}^l =&\mathbf{T}\left(\mathbf{x}_{\text{pano}}; \Theta^l\right) \text{ and } \Delta\mathbf{x}_{\text{d}} \\ =&\mathbf{v}\left(\mathbf{x}_{\text{pano}}\right)\sum_{\mathbf{j}} B\left(\frac{\mathbf{x}_{\text{pano}}}{d_s} - \mathbf{j}\right)\Delta\theta_{\mathbf{j}}.\end{aligned} \tag{11}$$

Since $R_{\text{SDD}} > R_{\text{SAD}} - \left(\mathbf{x}_{\text{d}}^l - \mathbf{r}_{\phi_i}\right)\cdot\mathbf{b}_{\phi_i} >> \Delta\mathbf{x}_{\text{d}}\cdot\mathbf{b}_{\phi_i}$, we can approximate Eq. (10) without loss of generality to

$$\begin{aligned}\mathbf{A}_{\phi_i}\left(\mathbf{x}_{\text{d}}^l - \mathbf{r}_{\phi_i} + \Delta\mathbf{x}_{\text{d}}\right) \cong &\mathbf{A}_{\phi_i}\left(\mathbf{x}_{\text{d}}^l - \mathbf{r}_{\phi_i}\right) \\ &+ \frac{R_{\text{SDD}}}{R_{\text{SAD}} - \left(\mathbf{x}_{\text{d}}^l - \mathbf{r}_{\phi_i}\right)\cdot\mathbf{b}_{\phi_i}} \\ &\left[\Delta\mathbf{x}_{\text{d}}\cdot\mathbf{a}_{\phi_i} \quad \Delta\mathbf{x}_{\text{d}}\cdot\mathbf{a}_z\right]^T.\end{aligned} \tag{12}$$

Subsequently, we apply the first-order Taylor series expansion to P_{ϕ_i} in Eq. (4), as follows:

$$\begin{aligned}P_{\phi_i}\left(\mathbf{A}_{\phi_i}\left(\mathbf{x}_{\text{d}}^l - \mathbf{r}_{\phi_i} + \Delta\mathbf{x}_{\text{d}}\right)\right) \cong &P_{\phi_i}\left(\mathbf{A}_{\phi_i}\left(\mathbf{x}_{\text{d}}^l - \mathbf{r}_{\phi_i}\right)\right) \\ &+ U_i^l\left(\mathbf{x}_{\text{pano}}\right) \\ &\sum_{\mathbf{j}} B\left(\frac{\mathbf{x}_{\text{pano}}}{d_s} - \mathbf{j}\right)\Delta\theta_{\mathbf{j}},\end{aligned} \tag{13}$$

where

$$\begin{aligned}U_i^l(\mathbf{x}_{\text{pano}}) =&\nabla P_{\phi_i}\left(\mathbf{A}_{\phi_i}\left(\mathbf{x}_{\text{d}}^l - \mathbf{r}_{\phi_i}\right)\right)^T \\ &\frac{R_{\text{SDD}}}{R_{\text{SAD}} - \left(\mathbf{x}_{\text{d}}^l - \mathbf{r}_{\phi_i}\right)\cdot\mathbf{b}_{\phi_i}} \\ &\left[\mathbf{v}\left(\mathbf{x}_{\text{pano}}\right)\cdot\mathbf{a}_{\phi_i} \quad \mathbf{v}\left(\mathbf{x}_{\text{pano}}\right)\cdot\mathbf{a}_z\right]^T.\end{aligned} \tag{14}$$

Substituting Eqs. (13) into (4), we define the linearized data term, D_{L} as follows:

$$\begin{aligned}D_{\text{L}}\left(\Delta\Theta; \Theta^l\right) = &\sum_i \sum_{\mathbf{x}_{\text{pano}}\in\Omega_i} \left\| P_{\phi_i}\left(\mathbf{A}_{\phi_i}\left(\mathbf{x}_{\text{d}}^l - \mathbf{r}_{\phi_i}\right)\right)\right. \\ &- P_{\phi_{i+F}}\left(\mathbf{A}_{\phi_{i+F}}\left(\mathbf{x}_{\text{d}}^l - \mathbf{r}_{\phi_{i+F}}\right)\right) \\ &+ \left(U_i^l\left(\mathbf{x}_{\text{pano}}\right) - U_{i+F}^l\left(\mathbf{x}_{\text{pano}}\right)\right) \\ &\left.\sum_{\mathbf{j}} B\left(\frac{\mathbf{x}_{\text{pano}}}{d_s} - \mathbf{j}\right)\Delta\theta_{\mathbf{j}}\right\|_2^2.\end{aligned} \tag{15}$$

Since D_{L} is a non-separable function of multiple unknowns, it is not suitable for parallel processing. We hence derive a separable surrogate function of D_{L} based on the optimization transfer method. Namely,

$$\begin{aligned}D_{\text{S}}\left(\Delta\Theta; \Theta^l\right) = &\sum_i \sum_{\mathbf{x}_{\text{pano}}\in\Omega_i} \sum_{\mathbf{j}} B\left(\frac{\mathbf{x}_{\text{pano}}}{d_s} - \mathbf{j}\right) \\ &\times \left\| P_{\phi_i}\left(\mathbf{A}_{\phi_i}\left(\mathbf{x}_{\text{d}}^l - \mathbf{r}_{\phi_i}\right)\right)\right. \\ &- P_{\phi_{i+F}}\left(\mathbf{A}_{\phi_{i+F}}\left(\mathbf{x}_{\text{d}}^l - \mathbf{r}_{\phi_{i+F}}\right)\right) \\ &\left.+\left(U_i^l\left(\mathbf{x}_{\text{pano}}\right) - U_{i+F}^l\left(\mathbf{x}_{\text{pano}}\right)\right)\Delta\theta_{\mathbf{j}}\right\|_2^2,\end{aligned} \tag{16}$$

which satisfies the following three conditions[19,20]:

$$D_{\text{L}}\left(\Delta\Theta; \Theta^l\right)\big|_{\Delta\Theta=\mathbf{0}} = D_{\text{S}}\left(\Delta\Theta; \Theta^l\right)\big|_{\Delta\Theta=\mathbf{0}}, \tag{17}$$

$$\frac{d}{d\Delta\Theta} D_{\text{L}}\left(\Delta\Theta; \Theta^l\right)\Big|_{\Delta\Theta=\mathbf{0}} = \frac{d}{d\Delta\Theta} D_{\text{S}}\left(\Delta\Theta; \Theta^l\right)\Big|_{\Delta\Theta=\mathbf{0}}, \tag{18}$$

$$D_{\text{L}}\left(\Delta\Theta; \Theta^l\right) \le D_{\text{S}}\left(\Delta\Theta; \Theta^l\right). \tag{19}$$

We can easily note that Eqs. (17) and (18) are satisfied. Since the B-spline interpolation is a convex combination of B-spline coefficients, we also note that Eq. (19) is satisfied.[21] Meanwhile, the separable surrogate function of R can be written as Ref. [20].

$$\begin{aligned}R_{\text{S}}\left(\Delta\Theta; \Theta^l\right) = &\sum_{\mathbf{j}} \sum_{\mathbf{k}\in K_{\mathbf{j}}} \left\{\frac{1}{2}\left\| < \theta_{\mathbf{j}}^l + 2\Delta\theta_{\mathbf{j}} - \theta_{\mathbf{k}}^l\right\|_2^2\right. \\ &\left.+\frac{1}{2}\left\|\theta_{\mathbf{j}}^l - \theta_{\mathbf{k}} - 2\Delta\theta_{\mathbf{k}}^l\right\|_2^2\right\}.\end{aligned} \tag{20}$$

Combining Eqs. (16) and (20), we can redefine the cost function, which is suitable for parallel processing, as

$$C_{\text{S}}\left(\Delta\Theta; \Theta^l\right) = D_{\text{S}}\left(\Delta\Theta; \Theta^l\right) + \lambda R_{\text{S}}\left(\Delta\Theta; \Theta^l\right). \tag{21}$$

By setting the partial derivative of Eq. (21) with respect to each control point parameter to zero, the update amount at

each iteration step l can be obtained concurrently at each control point as

$$\Delta\hat{\theta}_j = -\frac{D' + \lambda R'}{D'' + \lambda R''}, \tag{22}$$

where

$$\begin{aligned} D' &= 2\sum_i \sum_{\mathbf{x}_{\text{pano}} \in \Omega_i} B\left(\frac{\mathbf{x}_{\text{pano}}}{d_s} - \mathbf{j}\right)\left(U_i^l(\mathbf{x}_{\text{pano}}) - U_{i+F}^l(\mathbf{x}_{\text{pano}})\right) \\ &\quad \left(P_{\phi_i}\left(\mathbf{A}_{\phi_i}\left(\mathbf{x}_{\text{d}}^l - \mathbf{r}_{\phi_i}\right)\right) - P_{\phi_{i+F}}\left(\mathbf{A}_{\phi_{i+F}}\left(\mathbf{x}_{\text{d}}^l - \mathbf{r}_{\phi_{i+F}}\right)\right)\right) \\ D'' &= 2\sum_i \sum_{\mathbf{x}_{\text{pano}} \in \Omega_i} B\left(\frac{\mathbf{x}_{\text{pano}}}{d_s} - \mathbf{j}\right)\left(U_i^l(\mathbf{x}_{\text{pano}}) - U_{i+F}^l(\mathbf{x}_{\text{pano}})\right) \\ &\quad \left(U_i^l(\mathbf{x}_{\text{pano}}) - U_{i+F}^l(\mathbf{x}_{\text{pano}})\right) \\ R' &= 4\sum_{\mathbf{k} \in K_{\mathbf{j}}} \left(\theta_{\mathbf{j}}^l - \theta_{\mathbf{k}}^l\right) \text{ and } R'' = 8N_{K_{\mathbf{j}}}. \end{aligned} \tag{23}$$

In order to further reduce the computational complexity and handle a large displacement problem in the iteration, we adopt a multiresolution scheme.

2.B. Generation of panoramic radiographic image

Once a dynamic focal plane is estimated by determining the optimal parameters, as in the previous sub-section, a panoramic radiographic image can be obtained via 3D back-projection of log-transformed data P.[9–11] Namely,

$$\begin{aligned} f_{\text{pano}}(\mathbf{x}_{\text{pano}}) = &\frac{1}{\sum_{i' \in \Lambda_{\mathbf{x}_{\text{pano}}}} \Delta\phi_{i'}} \\ &\sum_{i \in \Lambda_{\mathbf{x}_{\text{pano}}}} P_{\phi_i}\left(\mathbf{A}_{\phi_i}\left(\mathbf{T}(\mathbf{x}_{\text{pano}}; \Theta) - \mathbf{r}_{\phi_i}\right)\right) \cdot \Delta\phi_i, \end{aligned} \tag{24}$$

where $\Delta\phi_i$ denotes the angular increment of the source at the i-th view angle, and $\Lambda_{\mathbf{x}_{\text{pano}}}$ denotes a set of view indices that contribute to reconstructing $\mathbf{x}_{\text{pano}}$. We note in Eq. (24) that the proposed algorithm easily generates a panoramic radiographic image corresponding to an arbitrary 3D focal plane since it is based on 3D back-projection. Meanwhile, since the filtering operation, such as Shepp-Logan filtering,[9,10] is not included in the image generation process, unlike in the conventional 3D CT image reconstruction, the intensity value may become higher as the projection data are accumulated. To prevent this increase in intensity, a normalization factor is used in Eq. (24).

2.C. Evaluation

We evaluate the proposed algorithm using a numerical phantom dataset and four clinical datasets. The projection data of clinical datasets are obtained using T1-CS of Osstem Implant Co., Ltd., and the scan protocol utilized in this clinical human study was approved by Korea National Institute for Bioethics Policy (KONIBP), Republic of Korea (P01-201808-11-003). The information regarding the static focal plane and the corresponding scanning geometry of the source-detector pair is provided by the manufacturer. In the numerical phantom study, the phantom is made using mathematical ellipsoids of different shapes to simulate the human dentition, and the corresponding datasets are generated based on a simulated system with the same specifications as in the clinical study. For each dataset, we reconstruct two panoramic radiographic images using a conventional static focal plane and the proposed dynamic focal plane, respectively. The image size is commonly set to 2320 × 1280 with a pixel size of 0.094 × 0.094 mm^2. For the focal plane estimation, d_s in Eq. (2) is heuristically set to 27 pixels, which correspond to approximately 5 mm. The total number of control points is thereby 89 × 51 in 2D panoramic radiographic image domain. The proposed algorithm is implemented using C and CUDA on a GPU platform. In order to improve the visibility of the dental structure, a simple unsharp masking scheme is applied as post-processing on all panoramic radiographic images.

3. RESULTS

3.A. Numerical phantom data

In this study, we design a numerical phantom using multiple tilted ellipsoids. As shown in Fig. 5, the phantom includes both normal and abnormal dentition models in the lower and upper jaws, respectively. The abnormality of dentition in the upper jaw is modeled by adjusting the tilting angle of two ellipsoids.

Figures 6(a) and 6(b) show the panoramic radiographic images obtained using the static and dynamic focal planes, respectively. We can easily observe in the figure that the proposed algorithm provides a panoramic radiographic image of improved quality, where the boundaries of all ellipsoids are well focused for both normal and abnormal dentitions of the lower and upper jaws. The 1D intensity profiles in Fig. 7 also demonstrate that the proposed algorithm improves the image sharpness.

For further evaluation, we illustrate the static and the estimated dynamic focal planes along with an image of the numerical phantom, as in Figs. 8(b) and 8(d). We can easily see that the estimated dynamic focal plane is nearly coincident with the abnormal dentition of the upper jaw, where z = 96, as well as the normal dentition of the lower jaw, where z = 32. Furthermore, 3D illustrations in Figs. 8(a) and 8(c), which represents the depths from the plane of y = 0 to the static and dynamic focal planes, respectively, show how the estimated dynamic focal plane varies in the 3D domain.

3.B. Clinical human data

In order to evaluate the proposed algorithm in a clinical situation, we apply it to the following four clinical datasets: H1 with the patient having a normal dentition, H2 with

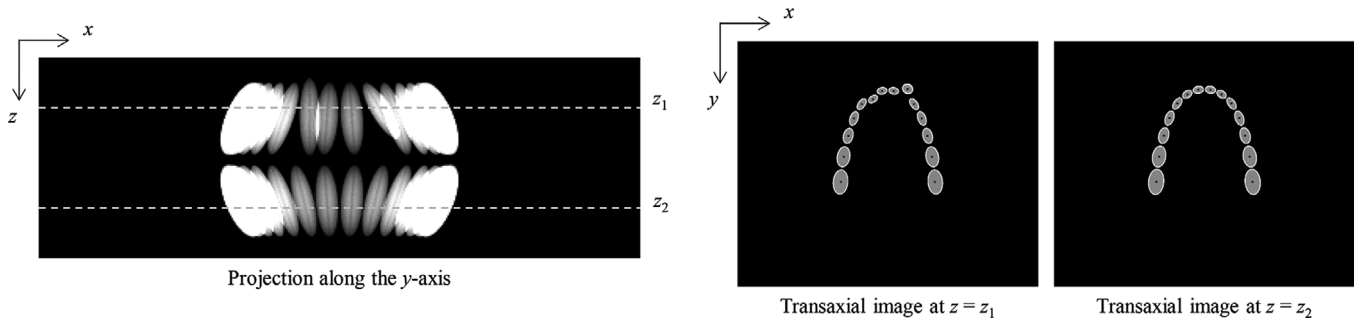

FIG. 5. Projection image of a numerical phantom along the y-axis; and two transaxial images of the phantom at upper and lower positions, respectively.

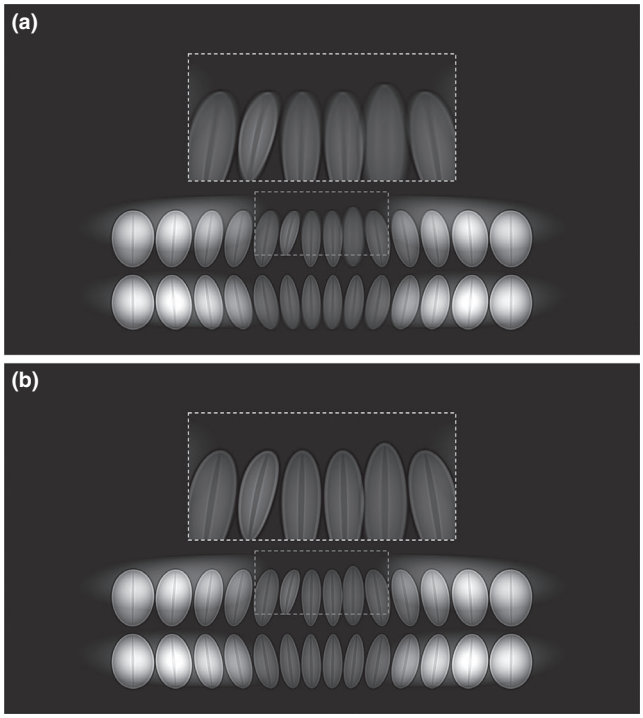

FIG. 6. Panoramic radiographic images of the numerical phantom obtained using (a) static and (b) estimated dynamic focal planes, respectively.

dentition having baby teeth, H3 with dentition including multiple metallic objects, and H4 with dentition having severely tilted teeth.

Figure 9 shows the panoramic radiographic images of H1 using the conventional static and estimated dynamic focal planes, respectively. As shown in the figure, the conventional static focal plane still provides acceptable image quality by showing sharp object boundaries throughout the image, because the intraoral structure of the patient in H1 is relatively well fitted to it. The estimated dynamic focal plane, however, provides further improved image quality in the enlarged areas.

On the other hand, for H2, the panoramic radiographic image of the conventional static focal plane fails to provide sharp object boundaries, unlike the image of the estimated dynamic focal plane, as shown in Fig. 10. This is because the dentition of the patient of H2 is too complex to be well represented using a simple static focal plane. Meanwhile, the proposed algorithm estimates the dynamic focal plane well such that it fits the patient's intraoral structure. It thereby provides improved image quality, especially in enlarged areas in Figs. 10(a) and 10(b).

Even though H3 includes multiple metallic objects, as shown in Fig. 11, the proposed algorithm improves the image quality by estimating the dynamic focal plane. The intraoral structures, especially around the fore teeth in the enlarged area, are blurred in Fig. 11(a), whereas those structures become sharper and clearly visible in Fig. 11(b).

Panoramic radiographic images of a patient having severely tilted teeth are obtained using H4, as shown in Fig. 12. As expected, we can easily see that the image quality is considerably improved using the proposed algorithm. Specifically, fore teeth with a large tilting angle, as well as the other intraoral structures, become sharper and more clearly visible.

For further evaluation, Fig. 13 shows 1D intensity profiles on enlarged areas of the panoramic radiographic images given in Figs. 9–12. It is noted in Fig. 13(c) that intensity profiles of the proposed dynamic focal plane provide higher resolution than those of ordinary static focal plane, especially at the points depicted by arrows where edges and small structures are located. In addition, any shift and/or magnification change are not noticeably observed between the intensity profiles of two images that are obtained using the static and dynamic focal planes, respectively.

4. DISCUSSIONS

In this paper, we propose an algorithm that can provide clear and focused digital panoramic radiographic images for patients having various dentitions. The proposed algorithm is based on the observation that the boundaries of the objects of interest, which are back-projected from each projection data, should be well aligned at the focal plane in order to obtain a clear and focused panoramic radiographic image. Accordingly, we newly introduce a dynamic 3D focal plane, which is well coincident with the objects, by describing its shape in the 3D space with a high DOF. We then derive an optimization process to determine the dynamic focal plane. In addition, for more reliable focal plane estimation, we propose a preprocessing method, which effectively alleviates undesirable effects of background objects in the projection data. The proposed algorithm is evaluated using simulation data and four clinical

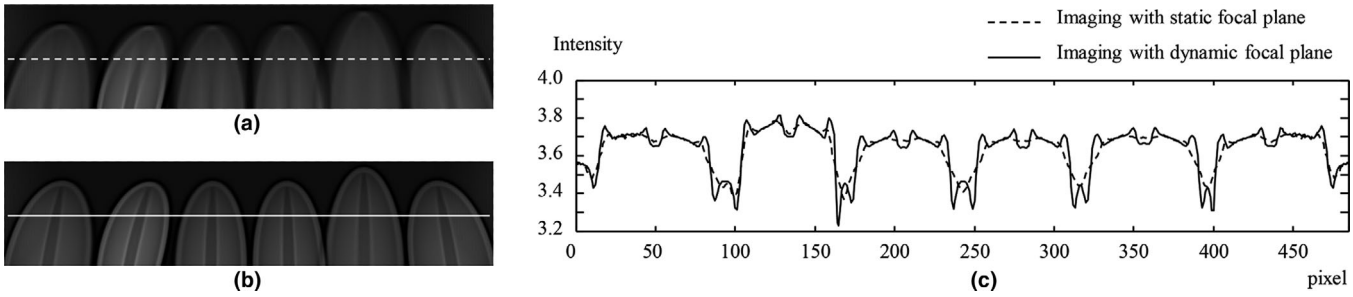

FIG. 7. Panoramic radiographic images of an enlarged region of interest that are obtained using (a) static and (b) estimated dynamic focal planes, respectively. (c) One-dimensional intensity profiles along the dashed and solid lines in (a) and (b), respectively. For better comparison, the noise in the profiles is reduced by averaging the intensities of 10 adjacent lines around the lines in (a) and (b), respectively.

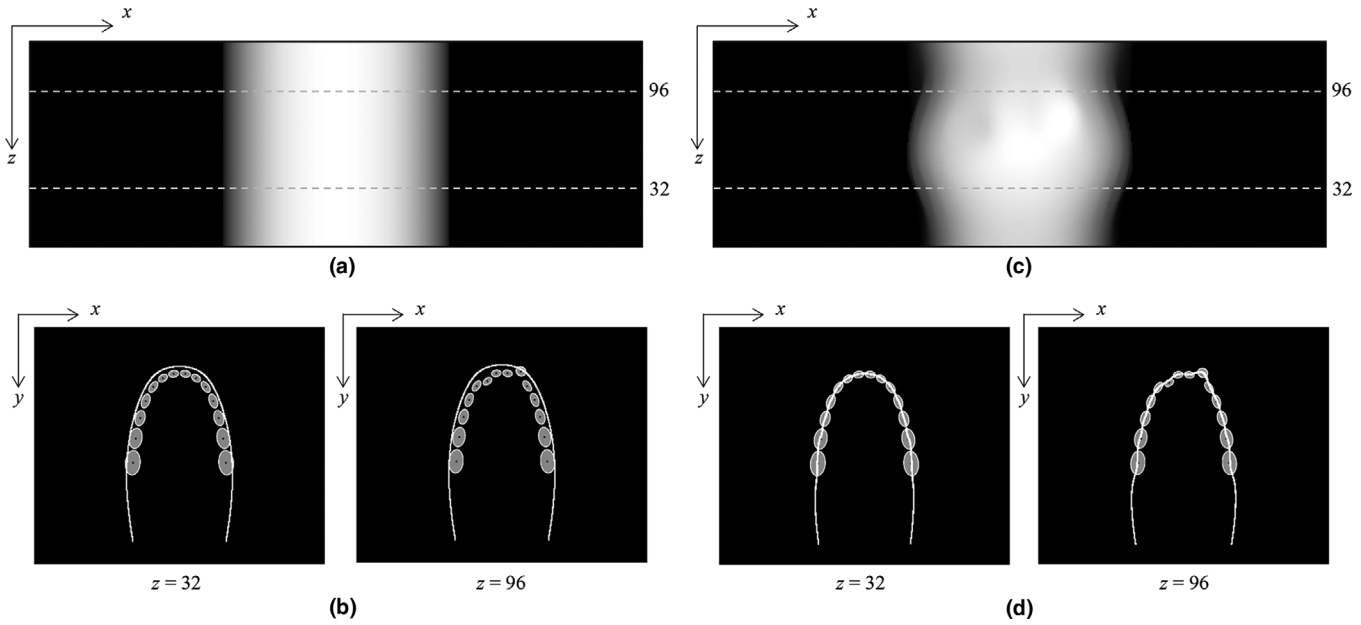

FIG. 8. (a) Three-dimensional illustration of the static focal plane; and (b) its transaxial views at z of 32 and 96, along with the corresponding transaxial images of the numerical phantom. (c) Three-dimensional illustration of the estimated dynamic focal plane; and (d) its transaxial views at z of 32 and 96, along with the corresponding transaxial images of the phantom. Note in (b) and (d) that transaxial views of focal planes appear as lines and their accuracy can be examined by referring to the transaxial images.

datasets. Experimental results show that the image quality is highly improved using the proposed algorithm.

Most previous algorithms to improve the image quality of panoramic radiography[4,6,7] select focused patches from the images, which are reconstructed at multiple parallel candidate focal planes. Hence, they need to determine the patch size and patch selection strategy, choose the number of candidate planes and a depth interval between candidate planes, and solve the discontinuity problem at the patch boundaries. Meanwhile, the proposed algorithm first introduces a more general focal plane model based on the *B*-spline and estimates its optimal model parameters via a continuous optimization. Hence, the proposed algorithm can guarantee a well-focused image over the whole region.

As shown in the results, the proposed algorithm improves the overall image quality by sharpening the boundaries of the other intraoral structures, such as the temporomandibular joint (TMJ), as well as the teeth. This is because the proposed algorithm introduces a generalized focal plane with high DOF in the 3D space by trying to align all boundaries of the objects that are back-projected from different view angles. Thereby, the proposed algorithm can improve the image quality throughout the image.

Meanwhile, a possible patient positioning error, which can be another reason for image quality degradation, is not considered in this paper. Like the proposed algorithm which estimates the patient's dentition based on the projection data, an advanced software approach may need to be developed to estimate and correct the patient positioning error for further improvement of image quality.

The proposed algorithm is suitable for parallel computing based on the GPU platform, because the optimization process consists of separable operations. The total computation time to obtain a panoramic radiographic image using the proposed algorithm is 6.5 s with a single GPU card, NVIDIA Tesla K40c. The computation time is not considered long for

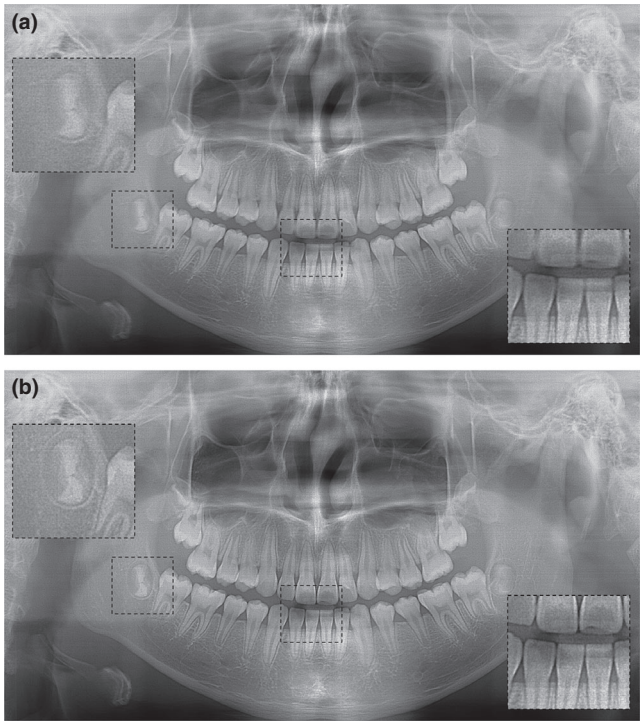

FIG. 9. Panoramic radiographic images reconstructed from clinical data H1, using (a) static and (b) estimated dynamic focal planes, respectively.

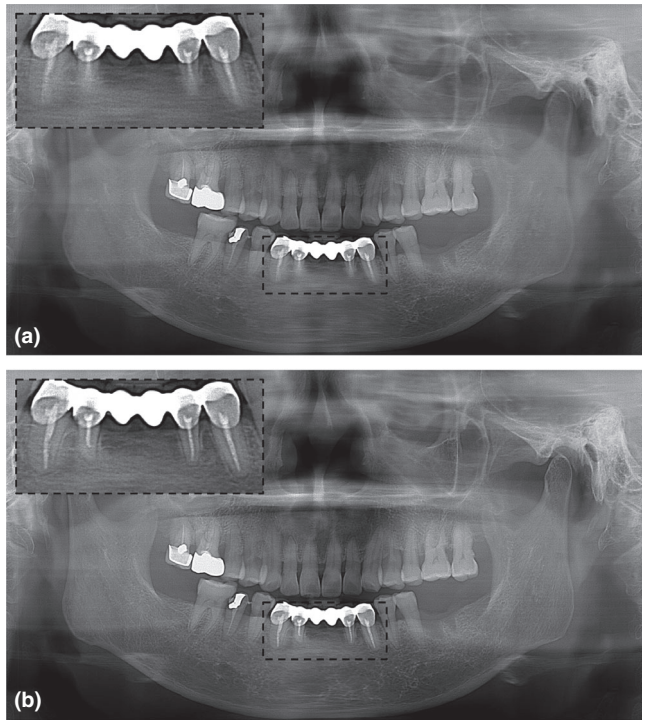

FIG. 11. Panoramic radiographic images reconstructed from clinical data H3, using (a) static and (b) estimated dynamic focal planes, respectively.

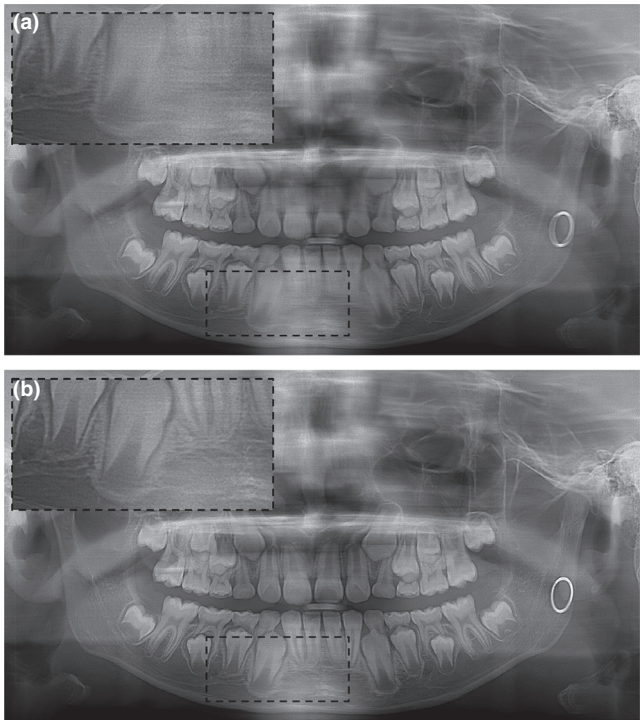

FIG. 10. Panoramic radiographic images reconstructed from clinical data H2, using (a) static and (b) estimated dynamic focal planes, respectively.

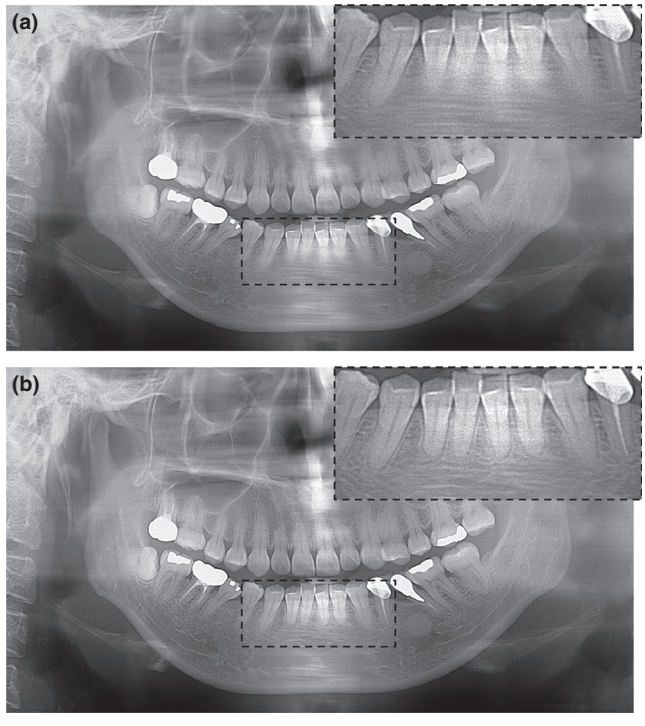

FIG. 12. Panoramic radiographic images reconstructed from clinical data H4, using (a) static and (b) estimated dynamic focal planes, respectively.

practical use, even though it takes 60 ms to obtain a conventional panoramic radiographic image in the same environment.

The feasibility and clinical applicability of the proposed algorithm are proven through the experiments in this paper. Nonetheless, for clinical use of the proposed algorithm, it is desirable to validate the proposed algorithm using extensive datasets with various clinical settings, as further work.

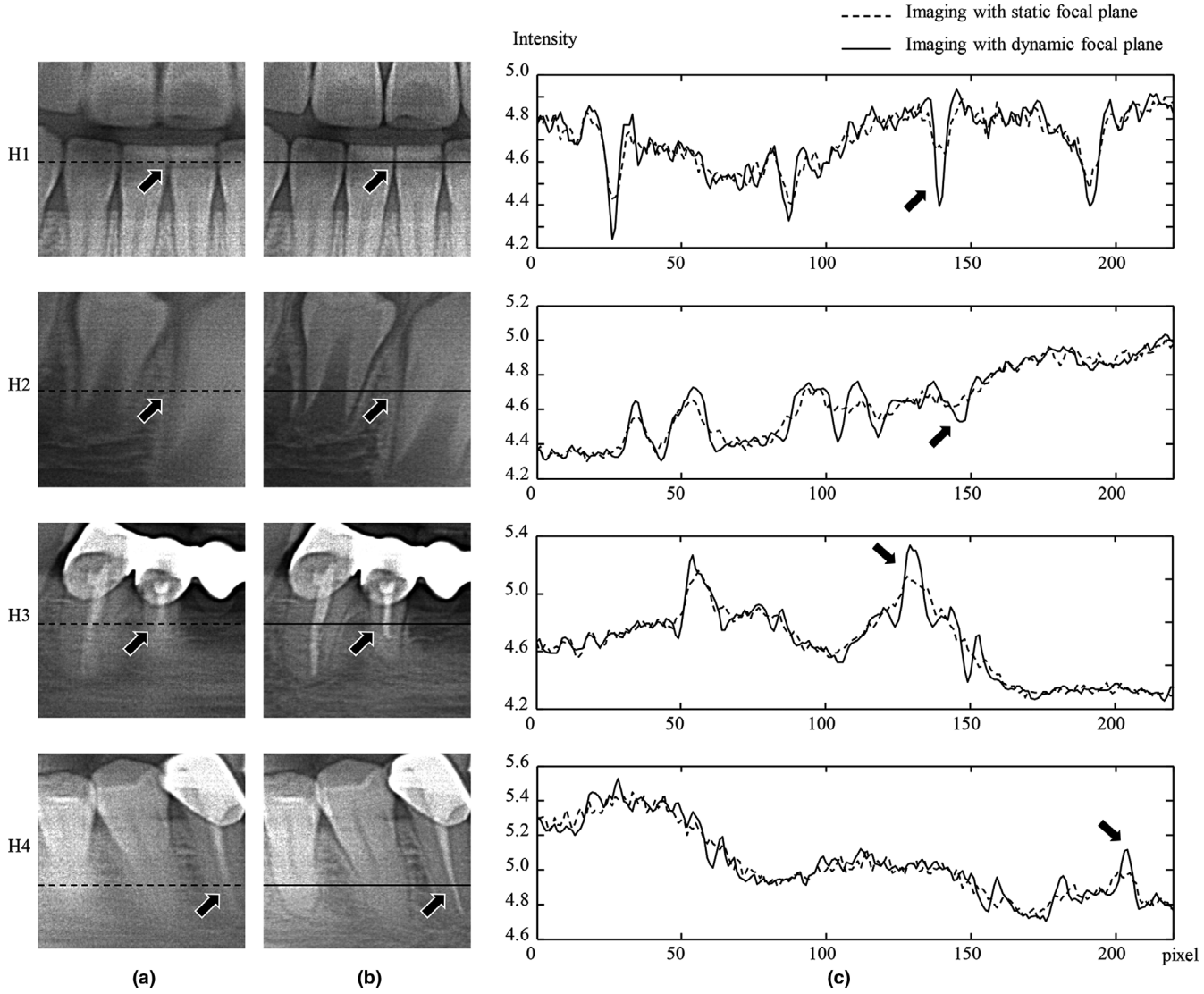

FIG. 13. Enlarged panoramic radiographic images for H1, H2, H3, and H4, which are obtained using (a) static and (b) estimated dynamic focal planes, respectively. Note that the pixel size is 0.094×0.094 mm^2. (c) The corresponding one-dimensional intensity profiles. For better comparison, the noise in the profiles is reduced by averaging the intensities of 10 adjacent lines around the lines in (a) and (b), respectively.

5. CONCLUSIONS

We propose an algorithm that can provide clear and focused panoramic radiographic images even for various types of dentitions, by estimating an adaptive dynamic focal plane. The proposed algorithm consists of three steps: preprocessing, dynamic focal plane estimation, and panoramic radiographic image reconstruction. The proposed algorithm is evaluated using a simulation dataset and four clinical datasets, and the results show that the algorithm can dramatically improve the image quality even for irregular dentitions.

ACKNOWLEDGMENTS

The authors thank Osstem Implant Co., Ltd. for providing financial support and clinical datasets for this work.

CONFLICT OF INTEREST

The authors have no relevant conflict of interest to disclose.

Seungeon Kim is currently with Samsung Advanced Institute of Technology (SAIT), Samsung Electronics Co., Suwon, Republic of Korea.
[a)]Author to whom correspondence should be addressed. Electronic mail: jbra@kaist.ac.kr.

REFERENCES

1. Hallikainen D. History of panoramic radiography. *Acta Radiol*. 1996;37:441–445.
2. Angelopoulos C, Bedard A, Katz JO, Karamanis S, Parissis N. Digital panoramic radiography: an overview. *Sem Orthod*. 2004;10:194–203.
3. Ogawa K, Langlais RP, McDavid WD, et al. Development of a new dental panoramic radiographic system based on a tomosynthesis method. *Dentomax Radiol*. 2010;39:47–53.

4. Katsumata A, Ogawa K, Inukai K, et al. Initial evaluation of linear and spatially oriented planar images from a new dental panoramic system based on tomosynthesis. *Oral Surg Oral Med Oral Pathol Oral Radiol Endodontol*. 2011;112:375–382.
5. Pawar RR, Makdissi J. The role of focal block (trough/plane) in panoramic radiography: why do some structures appear blurred out on these images? *Radiography.* 2014;20:167–170.
6. Lee T, Lee YJ, Cho S. Auto-focused panoramic dental tomosynthesis imaging with exponential polynomial based sharpness indicators. *Proc SPIE*. 2017;10133:101331Y.
7. Kitai N, Mukai Y, Murabayashi M, et al. Measurement accuracy with a new dental panoramic radiographic technique based on tomosynthesis. *Angle Orthod*. 2012;83:117–126.
8. Dobbins JT, Godfrey DJ. Digital x-ray tomosynthesis: current state of the art and clinical potential. *Phys Med Biol*. 2003;48:R65–R106.
9. Kak AC, Slaney M. *Principles of Computerized Tomographic Imaging*. New York: IEEE press; 1988.
10. Hsieh J. *Computed Tomography: Principles, Design, Artifacts, and Recent Advances*. Bellingham: SPIE; 2009.
11. Feldkamp LA, Davis LC, Kress JW. Practical cone-beam algorithm. *JOSAA*. 1984;1:612–619.
12. Bartolac S, Clackdoyle R, Noo F, Siewerdsen J, Moseley D, Jaffray D. A local shift-variant Fourier model and experimental validation of circular cone-beam computed tomography artifacts. *Med Phys*. 2009;36:500–512.
13. Pack JD, Yin Z, Zeng K, Nett BE. Mitigating cone-beam artifacts in short-scan CT imaging for large cone-angle scans. *Proc. Intl. Mtg. on Fully 3D Image Recon. in Rad. and Nuc. Med*; 2013:300–303.
14. Kim S, Chang Y, Ra JB. Cardiac motion correction based on partial angle reconstructed images in x-ray CT. *Med Phys*. 2015;42:2560–2571.
15. Unser M, Akram A, Murray E. Fast B-spline transforms for continuous image representation and interpolation. *IEEE Trans Pattern Anal Mach Intell*. 1991;13:277–285.
16. Lucas BD, Kanade T. An iterative image registration technique with an application to stereo vision. *Proc 7th IJCAI*. 1981;2:674–679.
17. Sotiras A, Davatzikos C, Paragios N. Deformable medical image registration: a survey. *IEEE Trans Med Imaging*. 2013;32:1153–1190.
18. De Pierro AR. A modified expectation maximization algorithm for penalized likelihood estimation in emission tomography. *IEEE Trans Med Imaging*. 1995;14:132–137.
19. Erdogan H, Fessler JA. Monotonic algorithms for transmission tomography. *IEEE Trans Med Imaging*. 1999;18:801–814.
20. Fessler JA, Sonka M, Fitzpatrick JM. Statistical image reconstruction methods for transmission tomography. *Proc SPIE*. 2000;2:1–70.
21. Kim S, Chang Y, Ra JB. Cardiac image reconstruction via nonlinear motion correction based on partial angle reconstructed images. *IEEE Trans Med Imaging*. 2017;36:1151–1161.